

ORBIT DETERMINATION USING A DECAMETRIC LINE-OF-SIGHT RADAR

G Frazer, M Rutten, B Cheung and M Cervera
National Security and ISR Division
Defence Science and Technology Organisation, AUSTRALIA
gordon.frazer@dsto.defence.gov.au

ABSTRACT

This paper investigates the effectiveness of a ground-based bistatic decametric line-of-sight radar for orbit determination of low Earth orbit satellites. Methods are developed for initial orbit determination. The approach is demonstrated using radar observations of the Hubble Space Telescope. The suitability of this class of radar for wide-field space situational awareness is considered, along with a SSA architecture that uses this class of radar to cue high-accuracy narrow field-of-view optical sensors as part of a wide-field high-accuracy system for SSA.

1 INTRODUCTION

This paper describes the use of high-frequency line-of-sight radar (HF-LOSR) to detect, track and establish an ephemeris of the Hubble space telescope (HST). While the HST is used as a case study in this paper, it is a target of opportunity and the radar's operation and the orbit determination procedures could be equally well applied to other satellites of interest, within the capabilities of the radar.

The radar has been developed by the Defence Science and Technology Organisation (DSTO) to investigate scattering phenomenology at HF frequencies. HF radars are typically deployed as over-the-horizon sensors, using the refractive properties of the earth's ionosphere for propagation beyond the line-of-sight horizon [1]. In contrast, the radar described in this paper has been designed for line-of-sight operation, using frequencies at the upper end of the HF spectrum to minimise ionospheric refraction. The radar has a wide field-of-view, having a 90° arc of coverage. While not being the radar's primary purpose, satellite transits are observed and specific measurement collections have been made of both the International Space Station (ISS) [2] and HST.

The radar measures range, Doppler and azimuth (coning angle). Two stages for orbit determination: extract associated detections from a potential target and then use those detections to calculate orbital parameters. Use a geometrical argument to form an initial orbit from two pairs of measurements of range and angle, separated in time. This orbit is then refined using the remainder of the measurements, including Doppler.

The paper is organised as follows. Section 2 is a description of the radar equipment. Section 3 describes the method for extracting target-associated detections from the radar data. A summary of the method used for initial orbit determination is given in Section 4, while Section 5 describes how that initial orbit is refined using the remaining measurements, including a comparison with the expected measurement from the publicly available TLE. Section 6 gives a preliminary analysis of measurement biases due to ionospheric effects. A summary of the results and an outline of future work is discussed in Section 7.

2 HF-LOS RADAR DESCRIPTION

The description of the HF Line-of-Sight Radar (HF-LOSR) in the following paragraphs relates to the particular configuration used in a test deployment in northern Australia undertaken by DSTO during 2013. Further details of this system, including energy budget, coverage calculations and predicted signal-to-noise ratio for the ISS can be found in a companion paper [2].

HF-LOSR is a bistatic high frequency radar designed to operate at a centre frequency selected between 29MHz and 31MHz depending on clear channel availability at the time of operation. The transmitter system was located approximately 1.8km from the receiver system. The radar used an amplitude tapered sweep linear frequency modulated continuous wave waveform with 100% duty-cycle. The operating bandwidth was 20KHz and the waveform repetition frequency (WRF) 100Hz. Total transmitter power was 16kW (continuous). The radar coherent integration time was 1s. The per-channel receiver system internal noise figure was 8dB and the external to internal noise ratio typically in the range 8-10dB depending on time-of-day ensuring that the receiver system was always externally noise limited. The receiver array used 20 receivers in a receiver per element configuration.



(a) Transmitter array.



(b) Receiver array.

Figure 1: Radar arrays used in HF-LOS. Each element is a four-element Yagi antenna optimised for operation in the frequency range from 29MHz to 31MHz.

The transmitter antenna consisted of a four element array where each element in the array consisted of a four-element Yagi antenna. The transmitter system comprised sixteen 1kW power amplifiers combined into four outputs, one for each element in the array. Each 1kW power amplifier was driven by an appropriate radar waveform generator. The spacing between elements was 10m for a total array aperture of 30m. The array spacing was such that the array was spatially undersampled by a factor of approximately two. The transmitter array is shown in the photograph in Fig. 1a which shows the upward tilt of the elements at an angle of approximately 55° with respect to the horizon.

The receiver antenna consisted of an array of 28 four-element Yagi antenna elements identical to the transmitter array elements with the exception of the feeder and feeder matching arrangements. The receiver array elements were spaced 9m apart so that the array was spatially undersampled. The antenna elements were connected to direct digital receivers in a receiver per element configuration. There was an additional receiver and vertical monopole antenna to provide spectrum surveillance for clear channel selection. The receiver per element arrangement allowed multiple simultaneous receiver beams to be formed and hence the receiver field of regard was covered simultaneously with full array gain. The receiver array is shown in the photograph in Fig. 1b.

Fig. 2 shows the effect of sphere size on RCS for a radar operating at 30MHz [3]. Spheres of diameter less than 2m are in the Rayleigh scattering region where RCS reduces dramatically as diameter is reduced. The resonance (or Mie) scattering region extends from sphere sizes of approximately 2m to 50m with the optical scattering region for sphere sizes larger than approximately 50m. To put this in context, the companion paper [2] predicts that this system could be capable of detecting objects in the order of 2m in physical size at 500km range and objects of approximately 4m at 1000km range.

3 TRACKING IN RADAR MEASUREMENT SPACE

As described in the introduction, the first step in reconstructing the orbit from HF-LOS observations was to extract detections associated with the target. While the target returns have typically large SNR, environmental effects, including ground clutter and background noise, result in false detections. In addition, the radar operational parameters are such that the Doppler returns are ambiguous, that is the target's range-rate cannot be directly inferred from the Doppler.

The tracking stage achieves two outcomes. Firstly, the output from the tracker is a set of detections which are likely to have originated from the same target, with a single detection per time-step. Secondly the Doppler ambiguity is resolved, such that the Doppler component of the associated detections can be interpreted as the range-rate of the target.

The algorithm used to achieve this is based on the probabilistic multi-hypothesis tracker (PMHT). PMHT is a data association algorithm derived from the application of the Expectation Maximisation (EM) algorithm [4] to target tracking. EM is used to model the assignment of measurements to targets as hidden variables and estimates target states by taking the expectation over the assignments [5]. The advantage of the PMHT over other conventional data association techniques is that it has linear complexity in the number of targets, the number of measurements per frame and in the number of frames, by assuming independence between the association hypotheses.

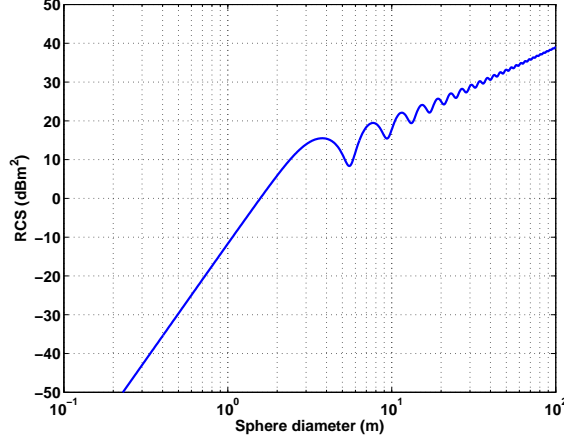


Figure 2: RCS of perfectly conducting spheres of varying diameters evaluated at a radar operating frequency of 30MHz.

Fig. 3 shows all of the radar detections for the observation period, for range, Doppler and coning angle, with those detections associated with the target in red.

4 INITIAL ORBIT DETERMINATION

The combination of range and coning angle, from two observation times, are used to calculate an initial circular orbit using a geometrical argument. By neglecting the Doppler measurement for initial orbit determination the resulting system has four measurement equations, which can be solved for the four orbital parameters. The initial solution can then be refined using the remainder of the data, as described in Section 5.

Define the relationship between the satellite position, \mathbf{p}_s , and velocity, \mathbf{v}_s , in geocentric Earth-fixed Cartesian coordinates, and measured range, ρ , range-rate, $\dot{\rho}$, and azimuth, α as

$$\rho = |\mathbf{p}_s - \mathbf{p}_{rx}| \quad (1)$$

$$\dot{\rho} = \frac{(\mathbf{p}_s - \mathbf{p}_{rx}) \cdot \mathbf{v}_s}{\rho} \quad (2)$$

$$\alpha = \arccos \left\{ \frac{(\mathbf{p}_s - \mathbf{p}_{rx}) \cdot \mathbf{u}_a}{\rho} \right\}, \quad (3)$$

where \mathbf{p}_{rx} is the radar receiver position, \mathbf{u}_a is a vector parallel to the receiver array, $\mathbf{a} \cdot \mathbf{b}$ is the vector dot product of \mathbf{a} and \mathbf{b} , and $|\mathbf{a}|$ is the magnitude of vector \mathbf{a} .

For a given measured range, ρ , and coning angle, α , the set of possible target locations trace out a circle in 3D, as shown in Figure 4. The equation for this circle can be defined by the centre of the circle

$$\mathbf{c} = \mathbf{p}_{rx} + \rho \cos(\alpha) \mathbf{u}_a, \quad (4)$$

the radius

$$r = \rho \sin(\alpha) \quad (5)$$

and a unit normal vector describing the plane of the circle, which in this case is given by \mathbf{u}_a , the vector along the array. These quantities can be rotated into an inertial coordinate frame in order to calculate the orbital parameters.

For a circular orbit with a known orbital radius, the target location corresponding to a range and coning angle is given by the intersection of a sphere and the circle defined above. There are two solutions to this intersection problem, as outlined in Appendix A. In this case the radar is designed to minimise directive gain away from the array boresight. This allows one of the solutions, the solution “behind” the radar to be neglected. Thus, given a range, a coning angle and an orbital radius, the target location can be calculated unambiguously.

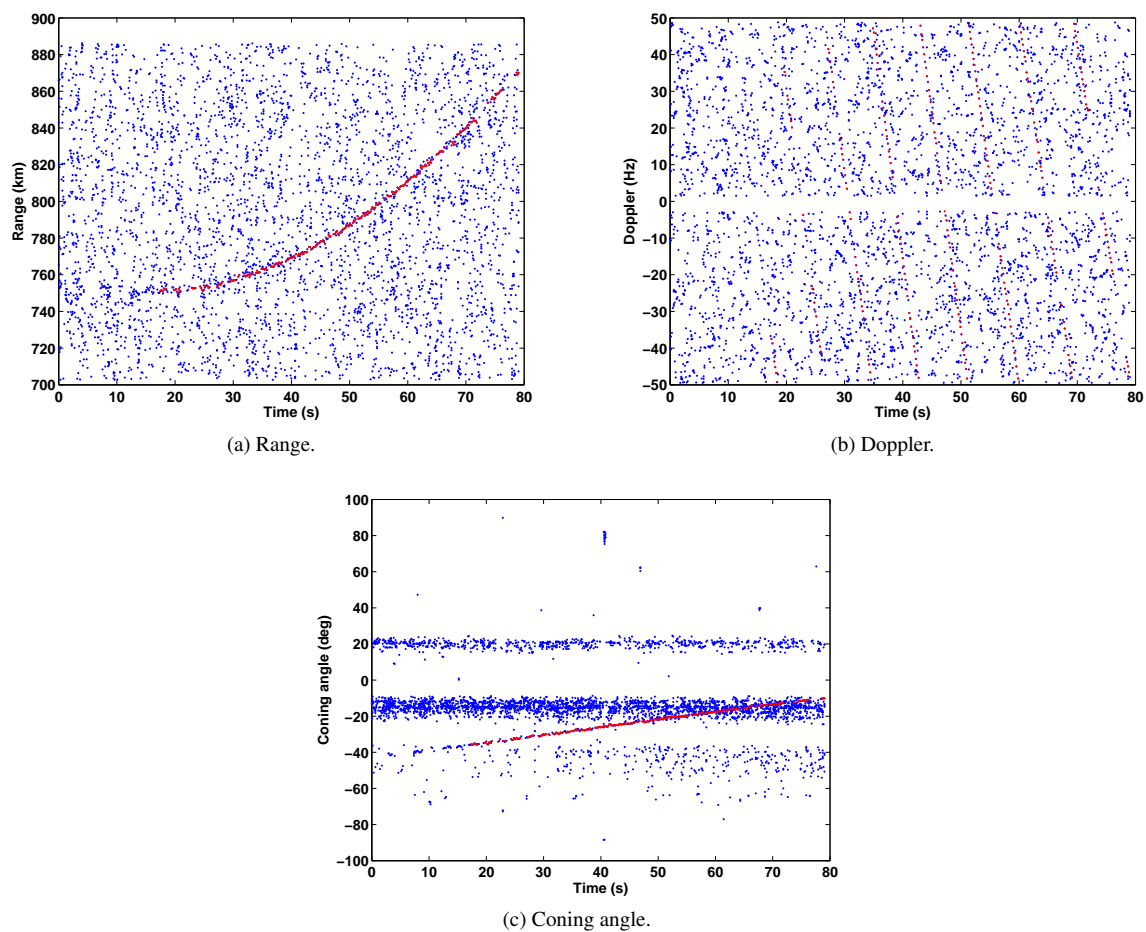


Figure 3: Associated detections (in red) and false alarms (in blue) for (a) range, (b) Doppler and (c) coning angle.

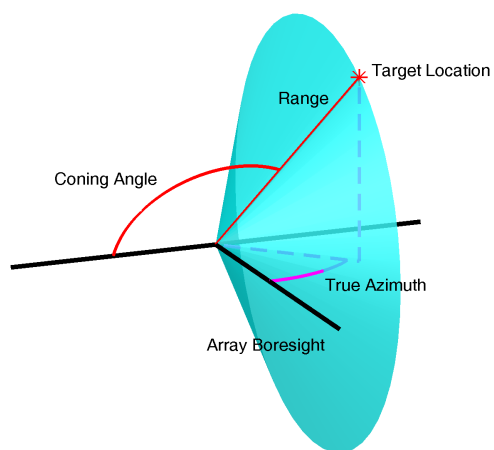


Figure 4: Coning angle: azimuth measured by a linear array.

Using two pairs of range/angle measurements gives two target locations at two instants in time, $\hat{\mathbf{p}}_{s1}$ and $\hat{\mathbf{p}}_{s2}$, assuming an orbital radius a . The circular orbit assumption means that the angle between these positions is directly related to the orbit's mean motion and hence the orbital radius.

$$\eta = \frac{1}{|t_2 - t_1|} \arccos \left\{ \frac{\hat{\mathbf{p}}_{s1} \cdot \hat{\mathbf{p}}_{s2}}{a^2} \right\} \quad (6)$$

$$a = \left(\frac{\mu}{\eta^2} \right)^{\frac{1}{3}}, \quad (7)$$

where t_1 and t_2 are the corresponding measurement times. The orbital radius can be found by solving (6) and (7) for a .

Since the solution to (6) and (7) is clearly not analytically tractable, the equations form the basis of a numerical algorithm for initial orbit determination. The steps of the algorithm are

1. Hypothesise an orbital radius, a , and calculate the circle-sphere intersection, $\hat{\mathbf{p}}_{s1}$ and $\hat{\mathbf{p}}_{s2}$, for both pairs of measurements.
2. Calculate the orbital radius, a' , equivalent to the mean motion implied by the two positions.
3. Use a numerical optimisation procedure to find a radius such that $a = a'$.
4. From the two position vectors calculate the velocity vectors, tangential to the orbit and in the plane of the orbit, with magnitude given by the *vis-viva* equation [6].

5 REFINING THE INITIAL ORBIT

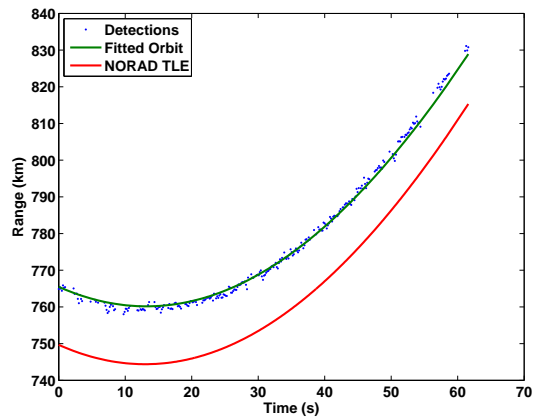
As described in the previous section, an initial orbit is calculated from two measurements, well-spaced in time to give range and azimuth diversity. This initial orbit is used as the starting condition for a least-squares (differential correction) procedure to refine the circular orbit using the entire batch of measurements. Unlike the initial orbit determination step, the refinement step uses Doppler (range-rate) along with range and coning angle. The SNR of the signal is used to calculate the expected accuracy of the measurement so that higher SNR detections are favoured over lower SNR detections in the least-squares fit. A Levenberg-Marquardt algorithm [7] has been used to perform the optimisation.

Results of the fitted orbit in this case are shown in Fig. 5, plotted against the radar measurements. It can be seen that the resulting orbit is consistent with the observations. However, when compared with the expected measurements from the NORAD TLE for the same time period, there is a bias of between 10 and 15km in range, up to 100m/s in range-rate and 1 to 2 degrees in angle. In Cartesian space these biases translate to a position error of between 21km and 29km and a velocity error of around 127m/s, shown in Fig. 6.

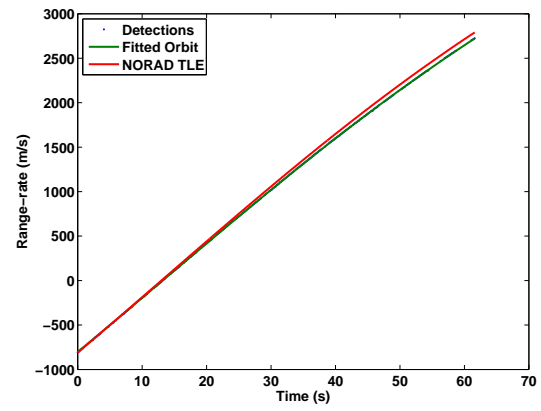
The differences between the observations and expected measurements are predominantly due to un-modelled sensor biases. While understanding and mitigating of these biases is an ongoing component of our research program, Section 6 addresses a major source of potential bias.

The accuracy of predictions made with the reconstructed orbit is important for queuing of narrow-field-of-view sensors. Differences between the predictions made with the fitted orbit and the NORAD TLE are plotted in Fig. 7, assuming that the TLE is a sufficient representation of the true orbit. Because of the circular orbit assumption and the unavoidable mismatch between the estimated orbital radius and the orbit's semi-major axis, the most significant error is an along-track error, which we have referred to as a timing error. A delay is calculated between the fitted orbit and the NORAD TLE in order to bring the predicted positions as close as possible. The plots in Fig. 7 show the timing error as a separate quantity. The remaining error is displayed using satellite-based NTW (radial, along-track, across-track) coordinates [6], where the along-track component points along the velocity vector. As a comparison, measurements have been simulated from the TLE, and the same orbital estimation procedure has been applied. This gives an indication of the best performance possible for this orbital estimation algorithm.

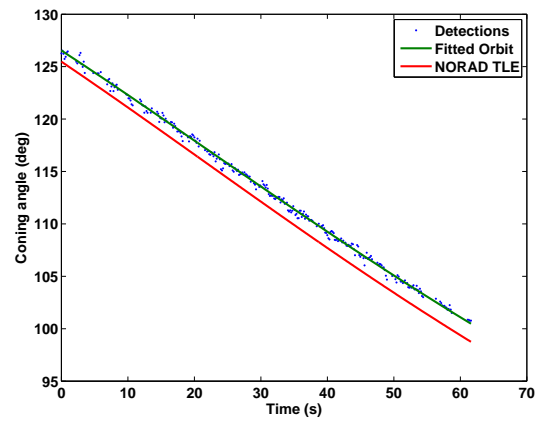
The results in Fig. 7 show that while the timing error increases steadily over time, the remaining error stays bounded over several orbital periods. It can also be seen that, despite the sensor biases evident in Fig. 5, the majority of the error in the predictions are due to the circular orbit constraint. In particular the radial error shows little deviation from the ideal case. Errors are periodic in the orbital period resulting in the smallest error at the same latitude as the radar.



(a) Range.

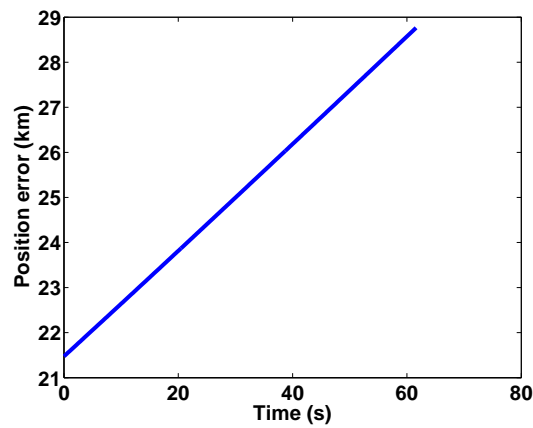


(b) Doppler.

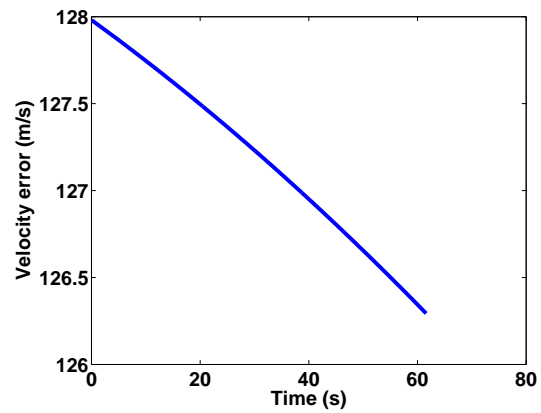


(c) Coning angle.

Figure 5: Target detections plotted along with the fitted circular orbit and the measurements expected according to the NORAD TLE.



(a) Position error.



(b) Velocity error.

Figure 6: Position and velocity errors between the fitted orbit and the the NORAD TLE.

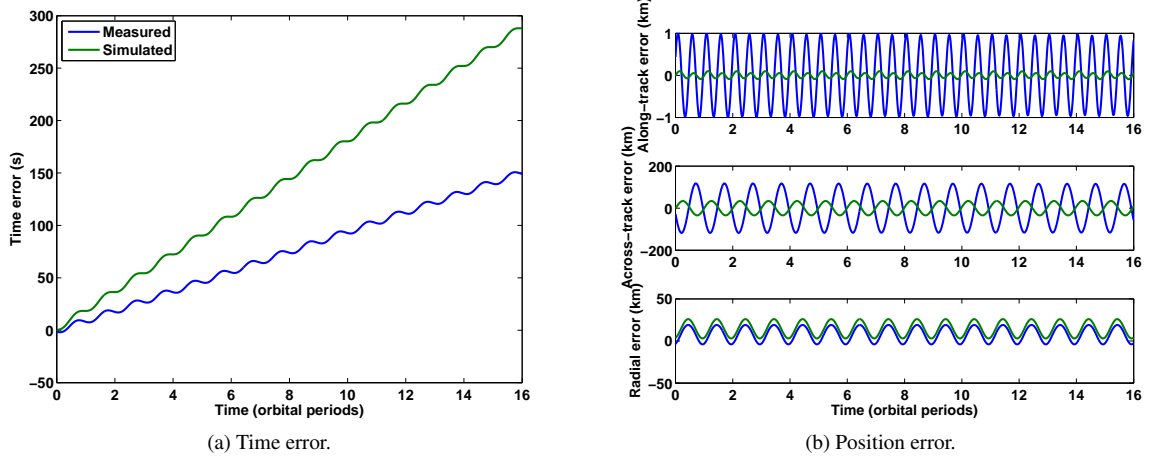


Figure 7: Prediction error between the fitted orbit and the NORAD TLE (blue), compared with an orbit fitted to simulated measurements from the TLE (green).

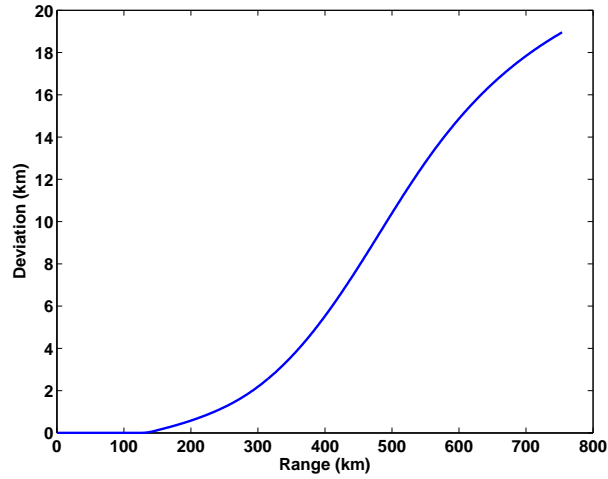


Figure 8: Distance between line-of-sight and a ray refracted through the ionosphere.

6 IONOSPHERIC BIAS EFFECTS

Most HF radars are designed to use the refractive properties of the ionosphere for over-the-horizon surveillance. The radar described in this paper uses a frequency toward the upper end of the HF band, typically around 30MHz, such that ionospheric refraction is minimised and line-of-sight operation can be achieved. The analysis in the preceding sections has assumed that the ionospheric refraction in this regime is negligible.

A preliminary investigation into the effects of the ionosphere at these frequencies has been conducted. For this purpose, the International Reference Ionosphere, IRI2012 [8], has been used to provide ionospheric and geomagnetic models. This model does not incorporate local measurements of the ionosphere, but is based on long-term historical data. So, while this model will give an indication of the lower-order effects of the ionosphere it will only be an approximation of the propagation conditions that existed at the time of the radar collection.

Modelling of HF propagation through the ionosphere is computed through the numerical integration of the underlying differential equations describing electromagnetic waves through a spatially varying plasma [9]. This is typically referred to as ionospheric ray-tracing. Fig. 8 shows the spatial separation between the direct line-of-sight calculation and a ray initialised with the same azimuth and elevation. It can be seen that as the ray approaches the target, there is a difference in position of about 19km. Ionospheric refraction is clearly not a negligible effect.

Rather than propagate a ray in the direction of the LOS path, the problem can be inverted, that is a ray direction can

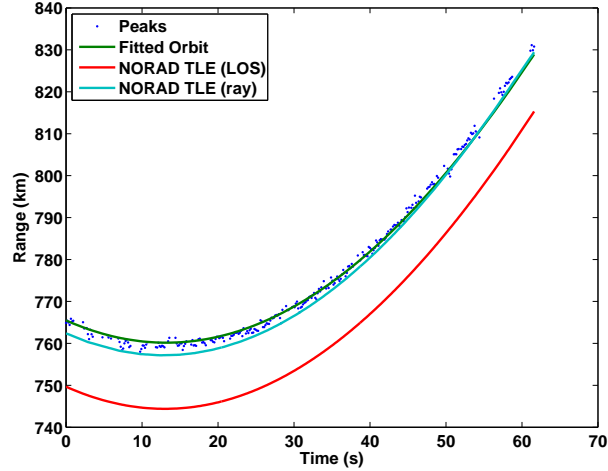


Figure 9: A comparison of the range measurements and the expected range from the TLE using direct line-of-sight and ionospheric refraction.

be found such that the ray intersects the satellite location. This method can be used to simulate radar measurements from the satellite position and velocity. The LOS mapping used to simulate radar measurements in the previous section can be replaced with a model that includes ionospheric refraction. Fig. 9 shows the range measurements of the HST plotted with the expected range from the NORAD TLE under LOS assumptions compared with using ionospheric ray-tracing. The effect of the refraction in this case is to reduce the range bias from over 10km down to less than 3km.

While this is a single example using a coarse model of the ionosphere, the results show that ionospheric effects could account for a significant component of the difference observed between the measurements and the TLE.

7 SUMMARY AND FUTURE WORK

This paper has presented a HF line-of-sight radar that is capable of detecting the Hubble space telescope. The companion paper concludes that this class of radar could be used for surveillance of space for objects of moderate size and range up to 1000km [2]. Automatic methods have been described for extracting detections associated with a potential satellite-like target and the determination of an orbit from those detections. In particular the techniques presented in this paper can be used for orbit determination using HF-LOSR without prior information, such as NORAD TLEs. The radar measurements, along with the orbit calculated from those measurements, shows significant differences to the published TLE. Analysis has shown that neglecting these biases, under the assumption that the TLE is consistent with the true orbit, results in an orbit with an approximately 20km separation from the published location.

Work in orbit determination with this class of radar will continue, including

- investigation of the ionospheric effects, including ray-tracing through a model ionosphere which uses measurements of local ionospheric conditions from vertical incidence sounders,
- investigation of the use of this type of radar to cue higher precision, but much lower field of regard, sensors to improve the estimates of the ephemeris, and
- more sophisticated estimation techniques, such as sequential Monte Carlo methods [10], which can capture the uncertainty in the resulting ephemeris.

ACKNOWLEDGEMENTS

The ionospheric ray-tracing results published in this paper were obtained using the Matlab HF propagation toolbox, PHaRLAP, created by Dr Manuel Cervera, Defence Science and Technology Organisation, Australia. This toolbox is available by request from its author (manuel.cervera@dsto.defence.gov.au).

REFERENCES

- [1] M. I. Skolnik, *Introduction to Radar Systems*. McGraw-Hill, third ed., 2001.
- [2] G. J. Frazer, D. H. Meehan, and G. M. Warne, “Decametric measurements of the ISS using an experimental HF line-of-sight radar,” in *Proceedings of the 2013 International Conference on Radar: RADAR 2013*, 2013.
- [3] E. Knott, J. Shaeffer, and M. Tuley, *Radar cross section: its prediction, measurement, and reduction*. Artech House, 1985.
- [4] A. Dempster, N. Laird, and D. Rubin, “Maximum likelihood from incomplete data via the EM algorithm,” *Journal of the Royal Statistics Society*, pp. 1–38, 1977.
- [5] R. Streit and T. Luginbuhl, “Probabilistic multi-hypothesis tracking,” *Technical report 10426, NUWC, Newport, Rhode Island, USA*, Feb 1995.
- [6] D. Vallado and W. McClain, *Fundamentals of Astrodynamics and Applications*. Microcosm Press, 2007.
- [7] O. T. K. Madsen, H.B. Nielsen, “Methods for non-linear least squares problems,” tech. rep., Technical University of Denmark, 2004.
- [8] D. Bilitza, L. McKinnell, B. Reinisch, and T. Fuller-Rowell, “The International Reference Ionosphere today and in the future,” *Journal of Geodesy*, vol. 85, no. 12, pp. 909–920, 2011.
- [9] K. Davies, *Ionospheric Radio*. London, UK: Peter Peregrinus Ltd., 1990.
- [10] A. Doucet, N. de Freitas, and N. Gordon, eds., *Sequential Monte Carlo Methods in Practice*. Springer, 2001.

A CIRCLE-SPHERE INTERSECTION

This section outlines an algorithm for finding the intersections of a circle in 3-dimensions and a sphere. The circle is defined by its centre \mathbf{c} , radius r lying on a plane with unit normal \mathbf{u} . The sphere is assumed to be centred at the origin with radius R .

For intersection points \mathbf{x} , lying on both the sphere and the circle

$$\mathbf{x} \cdot \mathbf{x} = R^2, \quad (8)$$

and

$$(\mathbf{x} - \mathbf{c}) \cdot (\mathbf{x} - \mathbf{c}) = r^2. \quad (9)$$

Since both \mathbf{x} and \mathbf{c} are on the plane of the circle, the projection of either of these vectors onto \mathbf{u} is the distance, α , from the origin to the plane, which can be written

$$\mathbf{x} \cdot \mathbf{u} = \mathbf{c} \cdot \mathbf{u} = \alpha. \quad (10)$$

Forming an orthogonal coordinate system in the circle’s plane using vectors $(\mathbf{c} - \alpha \mathbf{u})$ and $(\mathbf{u} \times [\mathbf{c} - \alpha \mathbf{u}])$ an equation for \mathbf{x} can be written as

$$\mathbf{x} = \alpha \mathbf{u} + \beta (\mathbf{c} - \alpha \mathbf{u}) + \gamma (\mathbf{u} \times [\mathbf{c} - \alpha \mathbf{u}]) \quad (11)$$

$$= (1 - \beta) \alpha \mathbf{u} + \beta \mathbf{c} + \gamma (\mathbf{u} \times \mathbf{c}). \quad (12)$$

Then (8) – (11) can be used to solve for β and γ . Taking the dot product of (12) with \mathbf{c} gives

$$\mathbf{x} \cdot \mathbf{c} = (1 - \beta) \alpha \mathbf{u} \cdot \mathbf{c} + \beta \mathbf{c} \cdot \mathbf{c} + \gamma (\mathbf{u} \times \mathbf{c}) \cdot \mathbf{c} \quad (13)$$

$$\beta = \frac{1}{2} \frac{R^2 - r^2 + |\mathbf{c}|^2 - 2\alpha^2}{|\mathbf{c}|^2 - \alpha^2}, \quad (14)$$

where (9) has been used to form an expression for $\mathbf{x} \cdot \mathbf{c}$. Now forming the dot product of both sides of (12)

$$\mathbf{x} \cdot \mathbf{x} = [(1 - \beta) \alpha \mathbf{u} + \beta \mathbf{c} + \gamma (\mathbf{u} \times \mathbf{c})] \cdot [(1 - \beta) \alpha \mathbf{u} + \beta \mathbf{c} + \gamma (\mathbf{u} \times \mathbf{c})] \quad (15)$$

which simplifies to

$$R^2 = (1 - \beta)^2 \alpha^2 + (1 - \beta) \alpha^2 \beta + (1 - \beta) \alpha^2 \beta + \beta^2 |\mathbf{c}|^2 + \gamma^2 |\mathbf{u} \times \mathbf{c}|^2 \quad (16)$$

$$\gamma^2 = \frac{R^2 - \alpha^2 + \beta^2 \alpha^2 - \beta^2 |\mathbf{c}|^2}{|\mathbf{u} \times \mathbf{c}|^2}. \quad (17)$$

To summarise, given vectors \mathbf{u} and \mathbf{c} and radii r and R the two points of intersection, \mathbf{x} , can be found using

$$\mathbf{x} = (1 - \beta) \alpha \mathbf{u} + \beta \mathbf{c} + \gamma (\mathbf{u} \times \mathbf{c}), \quad (18)$$

where

$$\alpha = \mathbf{u} \cdot \mathbf{c} \quad (19)$$

$$\beta = \frac{1}{2} \frac{R^2 - r^2 + |\mathbf{c}|^2 - 2\alpha^2}{|\mathbf{c}|^2 - \alpha^2} \quad (20)$$

$$\gamma = \pm \frac{\sqrt{R^2 - \alpha^2 + \beta^2 \alpha^2 - \beta^2 |\mathbf{c}|^2}}{|\mathbf{u} \times \mathbf{c}|}. \quad (21)$$

Note that if \mathbf{u} and \mathbf{c} are parallel, that is $\mathbf{c} = k \mathbf{u}$ for some scalar k , then there will be no solutions, or, for $k = \sqrt{R^2 - r^2}$ the circle will lie completely on the sphere, giving an infinite number of solutions. Similarly, the argument of the square-root in (21) must be positive for a geometric solution.